Journal of Materials Chemistry A

ROYAL SOCIETY OF CHEMISTRY

PAPER

View Article Online
View Journal | View Issue

Cite this: J. Mater. Chem. A, 2024, 12, 26749

High performance, binder-free electrodes with single atom catalysts on doped nanocarbons for electrochemical water splitting synthesized using one-step thermally controlled delamination of thin films†

Efrat Shawat Avraham,‡[ae] Bibhudatta Malik,‡[ae] Alina Yarmolenko,‡[ae] Rajashree Konar,[abe] Sergei Remennik,[c] Gili Cohen Taguri,[a] Sandro Zorzi,[d] Elti Cattaruzza,[d] Michael Yakov Hubner[a] and Gilbert Daniel Nessim*[ae]

Developing high performance catalysts for electrochemical water splitting is critical for an efficient and sustainable route to hydrogen production. For this, single-atom catalysts (SACs) are the best candidates, as they offer the highest atom efficiency. However, current methods to produce SACs involve a complex synthesis, often requiring multiple lengthy and expensive steps and yielding an insufficient density of single atoms. Here, we report a one-step chemical vapor deposition (CVD) synthesis to produce free-standing (FS) electrodes with Ni SACs on a matrix of sulfur-doped carbon nanofibers (CNFs), referred to as SACs@nanocarbon. The mechanism is based on a temperature-controlled delamination of thin films, with Au in contact with a SiO_2 substrate, leading to the nucleation and growth of SACs@nanocarbon. Advanced characterization methods indicate the presence of Ni and Au single atoms and larger gold aggregates on the CNF matrix surface. These non-platinum group metal (non-PGM) electrodes showed exceptional performance for the oxygen evolution reaction (OER) and hydrogen evolution reaction (HER). They performed for over 20 000 cycles with negligible change in overpotential at higher currents, with low onset overpotentials of 305 mV at 10 mA cm^{-2} for the OER and 40 mV at 17 mA cm^{-2} for the HER. The overpotential decreased to 195 mV at a current density of 100 mA cm^{-2}. Remarkably, the electrode performance improved over cycling, while gold was dissolving in the electrolyte. This novel synthesis yielding SACs@nanocarbon could pave the way for the development of non-PGM, high performance electrodes for many other electrocatalytic applications. Additionally, the new paradigm of temperature-controlled delamination of thin films could be used to synthesize new materials.

Received 7th July 2024
Accepted 8th August 2024

DOI: 10.1039/d4ta04701j

rsc.li/materials-a

Introduction

Green energy sources have the potential to meet the ever-expanding global energy demand, considering the limited reserves of fossil fuels and the pollution issues related to their exploitation.[1] Electrochemical water splitting is one of the best methods to produce molecular hydrogen (H_2), which can power high-performance fuel cell vehicles and offer solutions to our global energy crisis.[2,3] Electrocatalytic water splitting involves a cathodic hydrogen evolution reaction (HER) and an anodic oxygen evolution reaction (OER).[4] In practice, H_2 evolution is hindered by the sluggish kinetics of the OER, which requires a four-proton-coupled electron transfer (PCET) process.[5] Therefore, the OER is considered as the bottleneck of water electrolysis, involving complex adsorption and desorption of intermediates, thus requiring a larger overpotential to drive the anodic reaction (E^0 = 1.23 V *vs.* RHE).[6] Fortunately, the use of efficient and high-performance electrocatalysts can reduce the overpotential of the anodic OER. Currently, noble metal-based systems, such as IrO_2, RuO_2, and Pt, are used as state-of-the-art electrocatalysts for both the OER and the HER.[7,8] However, noble metal systems are not appropriate for large-scale applications due to their scarcity and high cost.[9] In this regard, single-atom catalysts (SACs) have emerged as a new class of OER

[a]Department of Chemistry and Institute of Nanotechnology and Advanced Materials (BINA), Bar-Ilan University, Ramat-Gan, 5290002, Israel. E-mail: gdnessim@biu.ac.il
[b]Atomic Structure-Composition of Materials, INL – International Iberian Nanotechnology Laboratory, Avenida Mestre José Veiga s/n4715-330, Braga, Portugal
[c]Center for Nanoscience and Nanotechnology, Hebrew University, Jerusalem 9190401, Israel
[d]Department of Molecular Sciences and Nanosystems, "Università Ca' Foscari Venezia", Via Torino 155, 30172 Venezia Mestre, Italy
[e]Israel National Institute of Energy Storage (INIES), Ramat-Gan 52900, Israel

† Electronic supplementary information (ESI) available. See DOI: https://doi.org/10.1039/d4ta04701j

‡ These authors have made equal contributions to this work.

electrocatalysts, as they offer 100% atom utilization and exhibit excellent catalytic behavior compared with traditional supported nanoparticles.[10,11]

The HER and OER performances of a wide variety of noble and non-noble metal SACs were examined in the literature.[12] Ni-, Co-, and Fe-based SACs on heteroatom-doped carbon systems showed highly efficient OER electrocatalysis in alkaline medium. Ni-doped carbon exhibited the best performance (followed by Co and Fe).[13,14] Unfortunately, producing high-density SACs presents many challenges as single atoms tend to aggregate into metal clusters to lower their surface energy during the synthesis.[15] Various strategies such as pyrolysis, chemical vapor deposition (CVD), atomic layer deposition, wet chemistry, atom trapping, and photochemical methods have been employed to limit this behavior.[16–19] However, these methods present clear drawbacks: pyrolysis produces carbon-based supports with uncontrollable and unpredictable structures due to the degradation of metal–organic complexes. Wet chemistry methods suffer from low SAC loading and a high possibility of aggregation of metal nanoparticles.[20] Atom trapping is a complicated process requiring high temperature, mobile atoms, and supports that can trap mobile species.[21] In most cases, the fabrication of electrodes requires many complex and expensive steps (*e.g.*, photolithography). Besides the above, the main issue is the low metal loadings that limit the commercial use of SACs.[14,22]

For practical applications, we need long-term stability and robustness of electrocatalysts, in addition to their electrocatalytic activity (*e.g.*, overpotential, kinetics, active surface area, faradaic efficiency, and turnover frequency). Electrodes based on powders need binders (*e.g.*, conducting polymers, mainly Nafion) for immobilizing the catalytic material on the current collector substrate. The issue with binders is that catalysts often peel off from the current collector during electrocatalysis, thus inhibiting long-term electrolysis and reducing current density.[23,24] This issue can be resolved by using free-standing (FS) electrodes, made of one material without any binder. Furthermore, bi-functional catalysts for the OER/HER can lower the production cost of electrodes for total water splitting, but obtaining high performance catalysts remains a challenge.[25]

Is it possible to synthesize high performance, non-PGM, free-standing, SA-based, bifunctional electrodes for water splitting using a simple and economical process?

Here we demonstrate a one-step process using CVD to produce free-standing electrodes, offers several advantages, both in terms of process simplicity and cost, and also in terms of good electrode performance and durability.

More specifically, we use CVD to synthesize bi-functional, self-standing electrodes made of SACs on a sulfur-doped nanocarbon matrix (SACs@nanocarbon) based on thermally controlled delamination of thin films of Ni and Au. We produced SACs@nanocarbon using a one-step chemical vapor deposition (CVD) synthesis that included four consecutive processes: (1) delamination of thin films from the substrate, (2) nucleation and growth of a nanocarbon mat, (3) formation of SACs, and (4) sulfur doping of the CNFs. This process is simple (one-step), economical, and industrially scalable (CVD).

The advantage of the electrodes produced is that they are bifunctional catalysts (OER and HER) and exhibit low overpotentials and extremely high cyclability (>20 000 cycles). The high conductivity of the sulfur-doped nanofiber carbon mat and its near super-hydrophobicity increase its electrical conductivity and facilitate the homogeneous diffusion of electro-active species and the weak interaction with water molecules further boosts the catalytic stability. The formed carbons are crystalline in nature, which makes them suitable for use as electrodes in water electrolysis and their extended conductive network accommodates single atoms (100% atom efficiency for catalytic reactions) to catalyze the HER and OER efficiently.

Experimental section

Synthesis of Au/Ni SACs on nanocarbon mats (C-10, C-30, C-60 and C-120)

Using electron beam (e-beam) evaporation, we deposited Au (50 nm) and Ni (100 nm) on a Si wafer with 1-micron SiO_2 without breaking vacuum. We then cut samples of 2.5 cm × 1 cm. Rutherford back scattering (RBS) measurements were taken to verify the thickness of the materials (Fig. S1†). We processed these samples using two atmospheric pressure CVD (AP-CVD) furnaces (Lindberg Blue TF55035C-1) in series equipped with a fused silica (quartz) tube (internal diameter of 22 mm) with gas flows regulated using electronic mass flow controllers (MKS model P4B) with a digital mass flow control unit (MKS model 247D).

We placed the sample in an alumina boat at the exit of the downstream furnace outside the heated zone. First, we purged the reactor with 100 [sccm] of He gas (99.9999%, Gas Technologies) at room temperature for 15 min until the furnace reached the desired temperature. We then introduced 100 [sccm] of He, 200 [sccm] of H_2 and 200 [sccm] of C_2H_4 to delaminate the thin film stack and to nucleate and grow the nanocarbon mat. Using the "*fast-heat*" technique described in our previous publication,[26] the sample was kept at room temperature still positioned outside the exit of the second furnace and entered the heated zone only when the furnace reached the desired temperature. We thus heated the sample without exposing it to a temperature ramp. When the furnace reached 800 °C, the boat with the sample was introduced into the heated zone by sliding the quartz tube and heating for the required duration (30 s to 2 h). At the end of the synthesis, the tube was pushed out to position the boat containing the wafer outside the heating zone in order to cool it under a He flow. We labeled the delaminated mats obtained after reacting for 10 min to 2 h as C-10 (10 min), C-30 (30 min), C-60 (1 h) and C-120 (2 h) (photographs in Fig. S2†).

Synthesis of Au/Ni SACs on sulfur doped CNF supports (S-C-10, S-C-30, S-C-60 and S-C-120)

We followed the same preparation procedure reported in the previous section, but with the addition of a second boat with sulfur powder in the upstream furnace, while the sample with the thin films was heated in the downstream furnace. We placed a ceramic boat with 1 g of sulfur powder (Alfa Aesar, 99.5%, 325

mesh) outside the first furnace upstream of the gas flow and a second boat with a 2.5 cm × 1 cm piece of SiO_2/Au (25–100 nm)/Ni (50–200 nm) outside the second furnace downstream of the flow.

We purged the system using 100 [sccm] of He (99.9999%) for 15 min while keeping the two boats at room temperature (outside the heated zones) until the furnace reached equilibrium at the desired temperatures in the two zones to fill the reactor with helium, thus removing all air. To grow the nanocarbon with the SACs, we shifted the quartz tube to put the second boat inside the downstream furnace for 30 s to 2 h while flowing 100 [sccm] of He, 200 [sccm] of H_2 and 200 [sccm] of C_2H_4 gases. After that, using an external magnet,[27] we introduced the boat with the sulfur powder (1 g, Alfa Aesar, 99.5%, 325 mesh) in the upstream furnace for 60 min under a flow of 100 [sccm] of He to transport the vaporized sulfur gas to the downstream furnace to react with the sample.

At the end of the synthesis, the boat with the sulfur was pulled out of the heated zone using the magnet and the quartz tube was pushed out to position again the boat containing the sample outside the heated zone to cool under a flow of helium. The sulfur-doped delaminated mats obtained after reacting for 10, 30, 60 and 120 min are labeled S-C-10, S-C-30, S-C-60 and S-C-120 (photographs in Fig. S2†).

Experimental setup for electrochemical water splitting

We carried out electrochemical experiments using a Biologic (*VSP-128*) potentiostat in a three-electrode cell. We initially tested catalysts in powder form. Powders are usually dropcast over a current collector, where Nafion, quaternary ammonium-based ionomers, FuMA-tech FAA-3 and Tokuyama AS-4 are used as binders for practical applications.[28,29] It is important to know that, despite the wide use of ionomer binders in the water electrolyzer and fuel cell industries, the use of binders is challenging. For example, particles of catalysts bonded with each other and attached to the current collector with a binder exhibit greater electron transfer resistance due to poor adhesiveness between the catalyst layer and the collector, which eventually reduces the catalytic activity.[30] For our powder samples, we ground the delaminated samples well with a pestle in a mortar and prepared the catalyst ink by adding 4 mg of powder catalysts to a mixture containing 600 μL of DI water, 350 μL of absolute ethanol and 50 μL of 5% Nafion solution and sonicating for about 45 min. We dropcast 8 μL of the ink over a 5 mm glassy carbon electrode (GCE) and left it to dry under ambient conditions. The catalysts loaded over the GCE served as the working electrode with Hg/HgO (filled with 1 M NaOH) and a Pt spiral as reference and counter electrodes, respectively. We utilized a RRDE 3A (ALS, Japan) for the rotation of electrodes in rotating disk electrode mode (RDE). Initially, *I–V* polarization was carried out by recording the cyclic voltammogram for 100 cycles with a sweep rate of 50 mV s^{-1}.

In a similar way, we took 10 mg of both RuO_2 and Pt/C and added them to a mixture of 500 μL of DI water, 400 μL of absolute ethanol 100 μL of 5% Nafion solution and sonicated for 30 minutes. 100 μL of each catalyst ink was dropcast on previously cleaned carbon papers (1 cm^2). Finally, the electrodes were dried and used for electrochemical studies.

Electrochemical impedance spectroscopy (EIS) is useful to understand charge transfer mechanisms during the electro-oxidation of water to O_2. Here, we varied the frequency in the range of 100 kHz to 100 mHz (a small perturbation of 10 mV). The potential scale as per the reversible hydrogen electrode (RHE) was calibrated to $E_{RHE} = E_{Hg/HgO} + 0.93$ V and thus we calculated the overpotential as $\eta = E_{RHE} - 1.23$ V. We carried out the OER and HER studies in 1 M KOH (pH 14) under ambient conditions with saturation of the electrolyte using argon gas. While testing our samples, we observed that only those synthesized for 1 or 2 h exhibited sufficient mechanical strength to be used as freestanding (FS) electrodes.

After synthesizing free-standing electrodes with sufficient mechanical strength for electrocatalysis and superior OER performance, we stopped using powders. These binder-free self-standing electrodes do not exhibit the issues mentioned above for powder-based/binder electrodes. We analyzed the OER and HER performance of the FS electrodes by electrochemical testing in a typical three-electrode setup with a PTFE replaceable holder as the current collector for the working platinum electrode (see the optical image in Fig. S10†). This one-step synthesis, without post-processing or coating, is carried out to avoid organic binders. The electroactive species with the conductive substrates exhibit good electronic conductivity and mechanical integrity as catalysts for long-term cycling.

In the ESI,† we provide additional details on the characterization methods we used, such as XRD, XPS, Raman, *etc.*, as described in the results section.

Results and discussion

We prepared high-performance, bi-functional, free-standing, electrodes with high-density SACs on carbon nanofibers for water splitting using CVD. First, Ni/Au thin films delaminate from the Si/SiO_2 substrate during thermal annealing, followed by the formation of a mat of CNFs in the presence of ethylene, the carbon precursor. In 2014, we demonstrated the delamination of a Ni/Pd film with a thin Ti adhesion layer from a Si/SiO_2 substrate to form a nanocarbon matrix.[31] However, this material did not form SACs on the CNFs and did not exhibit any electrocatalytic performance. Here, we chose gold as the thin film in contact with the substrate as it does not adhere well to silicon oxide.[32] The sample was heated in the presence of He, H_2, and C_2H_4 to nucleate and grow the nanocarbon matrix, upon which the SACs will then form. After the nanocarbon growth, we vaporized sulfur in the upstream furnace and carried it with a flow of He to the downstream furnace to dope the nanocarbon matrix. As a final product, we obtained a delaminated black mat with a slightly larger area than the substrate (Fig. 1). High-resolution scanning electron microscopy (HRSEM) of the delaminated samples shows entangled carbon nanofibers (CNFs) with micron-range diameters (Fig. 1). High-resolution transmission electron microscopy (HRTEM) of the CNFs in the doped sample is shown in Fig. S11.† Focused ion beam (FIB) measurements on a cross-section of the doped

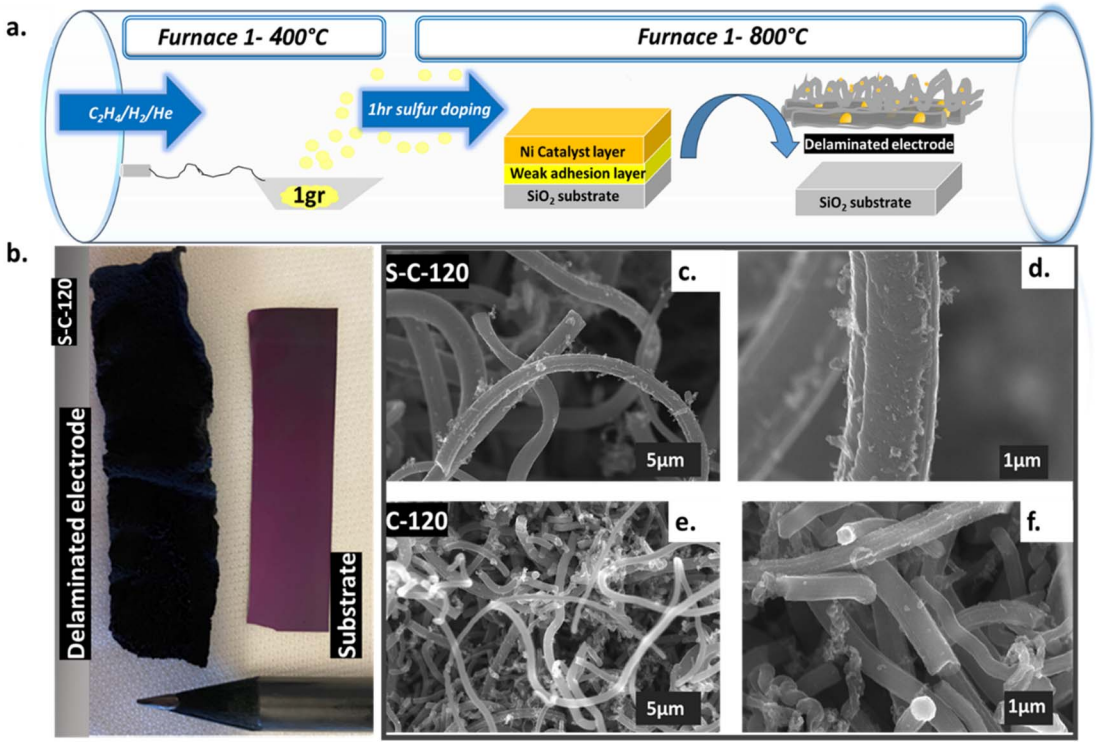

Fig. 1 (a) Schematic view of the equipment used for the synthesis. In the upstream furnace, we introduced the sulfur powder that vaporized and, was carried by an He flow, reached the downstream furnace, where the thin metal film stack delaminated from the substrate to grow the nanocarbon matrix with SACs on the CNFs. The temperatures used were 400 °C (T_1) and 800 °C (T_2). (b) Delaminated electrode (above) and substrate from which the thin film stack delaminated (below) for the free-standing sample grown for two hours. (c) HRSEM image (5000) of the sulfur doped sample after 2 h of growth. (d) Higher magnification of figure (c) (20 000×). (e) HRSEM image (5000×) of the undoped sample after 2 h of growth. (f) Higher magnification of figure (e) (20 000×).

sample and EDX measurements (Fig. S3 and S4†) indicate the presence of carbon, sulfur, nickel, and gold. The FIB cross-section also shows that the nickel content decreases as we get deeper into the sample, which correlates with the results obtained from X-ray photoelectron spectroscopy (XPS), where Ni was detected only when we positioned the sample upside down (Fig. S9†).

Raman spectroscopy measurements of S-C-120 show a G band peak at ~1580 cm^{-1} and a 2D band peak at ~2700 cm^{-1} (Fig. S5†). The ratio D/G = 1.08 indicates a graphitic structure, where the D band indicates a defect in the graphitic structure, which arises from out-of-plane vibration, while the G band originates from the in-plane vibration of the C–C bond from sp^2 hybridization.

We characterized the C-120 (Fig. S6a†) and S-C-120 (Fig.S6b†) samples using aberration-corrected HRTEM with high-angle annular dark-field imaging (HAADF-STEM) to achieve atomic resolution. We identify the bright dots circled in yellow in Fig. 2b as single or very few atoms that we will call single atom catalysts (SACs). We performed extensive electron dispersive spectroscopy (EDS) and subsequent mapping of the different elements on the S-C-120 sample (Fig. S7†). This mapping shows that the dots are made of Ni, Au, or possibly both (see Fig. S7c and e†) and that carbon and sulfur are uniformly distributed (Fig. S10d and f†). The dimensions of the SACs, in the range of Angstroms, are in agreement with previous reports of Ni SACs (and Fe) on different supports.[33] These data support the claims regarding the formation of well defined Ni SACs on the carbon matrix. Further, the HAADF imaging of the S-C-120 sample also reveals the presence of Au particles of around 200 nm in size (Fig. S8†). We characterized a cross-section (lamella) of the sample using a FIB to see how Ni penetrates the carbon material (Fig. S3†). Over a depth of around 10 microns, we observed that the concentration of nickel is at its lowest on the surface of the nanocarbon mat and increases with depth. This observation is consistent with XPS measurements (discussed later), where we only detected Ni at the bottom of the nanocarbon (*i.e.*, the part of the electrode in contact with the substrate before delamination), thus indicating that the amount of Ni on the surface of the nanocarbon increases with depth (Fig. S7†). We quantified the atomic content of nickel using inductively coupled plasma-mass spectrometry (ICP-MS) and it revealed that S-C-120 contains 2.6% Ni in it.

Fig. 2c shows the XRD pattern of C-120, S-C-120 and post-OER (S-C-120) samples. Each material showed four main broad peaks present at about 25.8°, 43.3°, 53.8° and 78.3° that correspond to the (002), (100), (004) and (110) planes of graphite, respectively. These strongly broadened peaks typically arise from their turbostratic character. As shown in Table 1, the (002) interlayer spacing for all samples is close to the characteristic

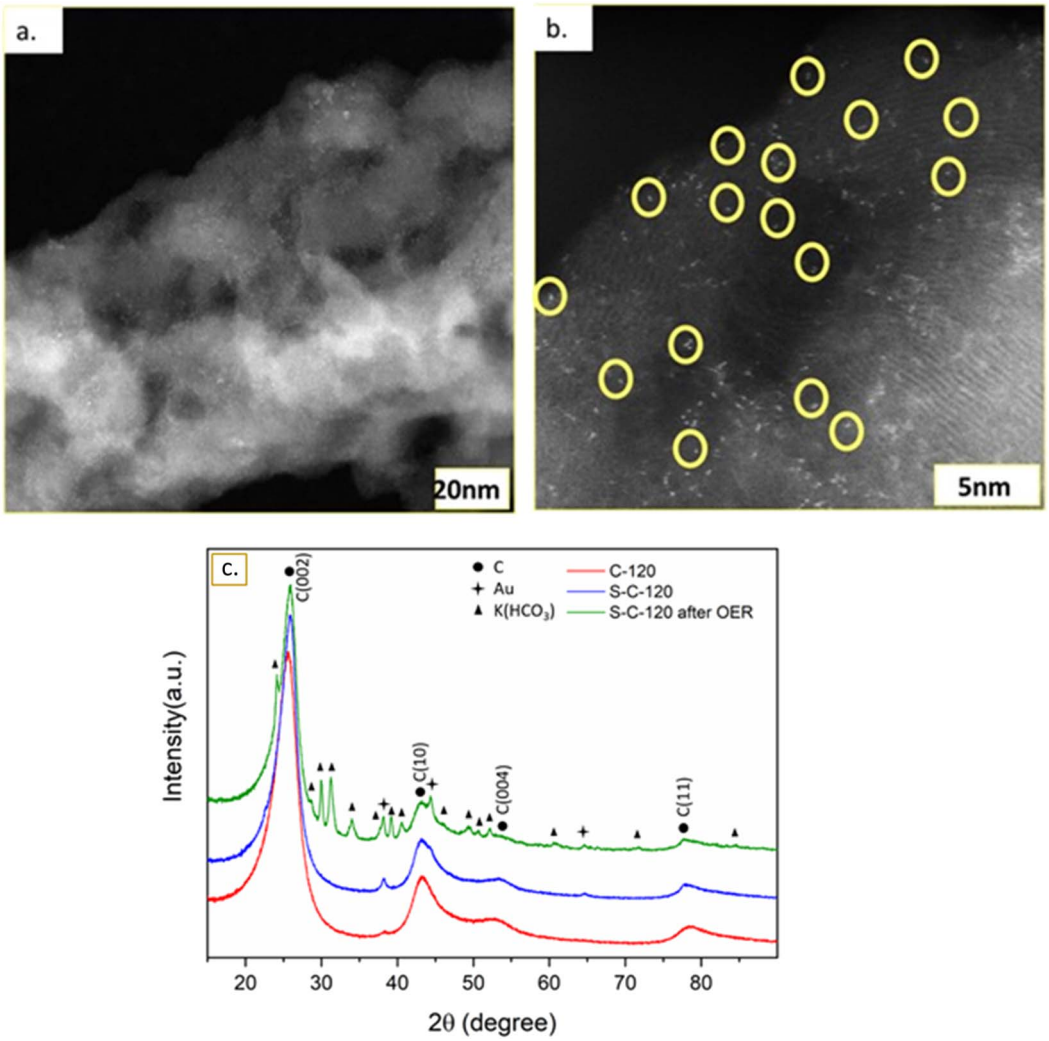

Fig. 2 (a) High-angle annular dark-field imaging (HAADF) of Ni-SACs grown on nanocarbon (S-C-120), (b) high resolution image showing the existence of atomically dispersed metals on crystalline carbon, and (c) powder XRD pattern of the three samples that were analyzed.

Table 1 Structural parameters (average interlayer spacing between carbon layers, d(002), and average size of basic structural units in the direction perpendicular to layers, L_c, obtained from the analysis of XRD patterns

Sample	d(002) [nm]	L_c [nm]
C-120	0.348	2.7
S-C-120	0.344	3.5
Post-OER, S-C-120	0.343	3.6

interlayer distance (0.344 nm) in turbostratic stacking. The diffraction peaks at 2θ of 38.1°, 44.3° and 64.5° correspond to the (111), (200) and (220) planes of Au (PDF #00-004-0784), respectively. After the OER, we observed the formation of the $K(HCO_3)$ phase (PDF# 01-086-0912) coming from the electrolyte. The XRD pattern suggested that no Ni phase was detected, further hinting that Ni was present only as single atoms. Structural parameters determined by quantitative analysis of the (002) peak are given in Table 1. The values of the interlayer spacing for d_{002} are calculated using Bragg's law as $d_{002} = n\lambda/2\sin\theta$, and the crystallite height (stack height) (L_c) is estimated *via* Scherrer's equation $L_c = 0.94\lambda/B\cos\theta$, where B is the FWHM and θ is the Bragg angle of the (002) band for L_c.[34] The sulfurization step clearly improved the graphitic order through the decrease of d_{002} and the increase of L_c for both S-C-120 and post-S-C-120. Lower values of d_{002} indicate fewer defects in the graphitic layers, leading to better packing of the carbon nanofibers.[35]

Using XPS, we probed the chemical states and bonding environments of the elements present in the doped samples. The C 1s spectrum in Fig. 6a reveals the presence of sp^2 hybridized carbon (peak position at 284.7 eV) and C–S bonding and π–π* transition as the deconvoluted peaks at 285.4 and 290.5 eV, respectively (Fig. S9a†).[36] The high-resolution spectrum of S 2p can be divided into S $2p_{3/2}$ and S $2p_{1/2}$ at 164.2 and 165.5 eV, respectively, attributed to the C–S linkage. An additional peak is observed at 168.5 eV due to SO_x bonding (Fig.

S9b†).[37,38] The core-level spectrum of Ni $2p_{3/2}$ is deconvoluted into three peaks positioned at 856.2, 861.5 and 862.8 eV, which can be assigned to high valence Ni (Ni^{3+}) and satellite peaks (Fig. S9c†).[39] Fig. S9d† illustrates the XPS spectrum of Au 4f, where two well-defined peaks at 84.1 and 88.1 eV correspond to Au $4f_{7/2}$ and Au $4f_{5/2}$, respectively, suggesting the existence of metallic Au.[40]

We also performed contact angle measurements (Fig. S10†). The contact angle of the non-doped sample was 128.7° compared to 143.2° for the sample doped with sulfur, indicating that the doped sample is more hydrophobic (almost superhydrophobic), which will be important for explaining the electrocatalytic performance.

The complex mechanisms leading to the formation of the SACs are difficult to precisely define without a dedicated *in situ* reactor that allows real-time characterization. This is compounded by several parameters playing a role, such as reaction time, temperature, amount of S doping, and the nature of the cooling procedure in this single-step CVD reaction. However, we can propose a plausible mechanism based on the extensive characterization performed.

The outstanding questions are mainly:

(1) Why do Ni and Au form SACs on the surface of the nanocarbon?

(2) Besides helping the delamination at high temperature, do Ni and Au contribute to the nucleation and growth of the carbon matrix?

(3) What is the role of sulfur? (As will be explained later, it significantly improved the electrocatalytic performance).

It is easy to understand that the Ni/Au thin film stack delaminates from the substrate owing to the weak adhesion of gold to Si/SiO_2. We can also hypothesize that the stack then fragmented into sub-micron particles that, in the presence of ethylene at high temperature, started nucleating and growing carbon nanofibers (Fig. 1). This is a plausible hypothesis given that Ni is a good catalyst for carbon nanotubes and nanofibers.[41,42] It is validated by our previous research, where we studied a delaminated layer of Ni/Pd weakly adhered to the silicon wafer with a very thin layer of Ti (as Pd does not adhere at all to Si/SiO_2), where, based on extensive characterization, we formulated a mechanism based on the fragmentation of the thin film into Ni/Pd alloy particles that led to nucleation and bidirectional growth of the nanofibers.[31] However, in that work, no metal atoms were present on the surface of the nanofibers, and the sample did not exhibit any electrocatalytic activity.

Here, we used Au as a weak adhesion layer and observed the formation of CNFs (as for Ni/Pd) but also found metal atoms on the surface of the carbon. We may explain this difference by observing and comparing the bulk phase diagrams of Ni–Pd and Ni–Au.§ The Ni–Pd phase diagram shows complete miscibility below 1237 °C for any composition. However, the Ni–Au phase diagram shows a synclinal miscibility gap with a peak at 807 °C at 72 at% Ni. From this, we can hypothesize the formation of two phases of the Ni–Au alloy during the thermal process with one phase slightly richer in Ni. Given that Ni is a known catalyst for CNF growth, we can speculate that one of the two phases is responsible for the nucleation and growth of the CNFs after fragmentation (similar to our previous work),[31] while the second phase "dewets" on the surface to form Ni and Au SACs.

The excellent electrocatalytic performance confirms that Ni SACs play a key role. However, regarding the Au SACs, we find gold in the solution during OER cycling (starting after 250 cycles and observed until 50 000 cycles), indicating that Au atoms on top of the carbon leach out to the electrolyte solution. Interestingly, the performance of the electrode increased during the leaching of the gold. Note that we also found larger gold chunks on the nanocarbon matrix that may also detach and dissolve into the electrolyte solution during electrocatalysis (Fig. S8†).

Let us now analyze the role of sulfur. Doping carbon nanomaterials is a practical and powerful approach to improve their properties, in particular their electrical conductivity.[43] Heteroatom-doped carbon nanotubes (CNTs) are studied in many fields, such as biotechnology, catalysis, optics, photovoltaics, supercapacitors, and energy storage. Based on the unique electronic properties and high surface area of CNTs, as well as the similar electronegativity of sulfur and carbon, Li *et al.*[44] prepared a novel electrocatalyst for the oxygen reduction reaction (ORR) by directly annealing oxidized CNTs and *p*-benzene dithiol in nitrogen. Previous studies demonstrated both experimentally and theoretically that heteroatom-doped CNTs can be regarded as a promising electrocatalyst for the OER.[38]

In our research, we also chose to dope our material with sulfur. Previous reports reveal that the inclusion of sulfur atoms in the carbon lattice may regulate the charge redistribution by tuning the electronic structure of the catalytic center, where adsorbates such as OOH*, O* and OH* prefer to adsorb.[45] We evaluated the samples with and without doping and observed that the electrocatalytic performance of the S-doped electrode was always far superior. We believe that the increased electrical conductivity and hydrophobicity due to sulfur doping are responsible for the improved electrochemical performance. Earlier research shows that the doping of S atoms in the carbon lattice has a great impact on the electronic structure and spin density and generates a significant number of active sites on carbon atoms, thus exhibiting improved electrocatalytic activities compared to pristine carbon samples.[46]

Oxygen evolution reaction (OER)

Initial experiments with powders on a substrate using binders showed poor performance. We first tested the powder by grinding the non-doped samples for various growth durations (10, 30, 60, and 120 min). Their comparative linear sweep voltammetry (LSV; Fig. S11a†) showed that C-10, C-30 and C-120 exhibited almost the same onset overpotential of 330 mV, while C-60 exhibited 370 mV. C-10 and C-120 delivered a current density of 10 mA cm^{-2} at overpotentials of 430 and 470 mV, respectively, while C-30 and C-60 failed to deliver a higher current.

§ Although our metallic films are tens of nanometers thick, which could lead to melting point depression or other phenomena that differ from the bulk, we will use as a first approximation the bulk phase diagrams to hypothesize the growth mechanisms.

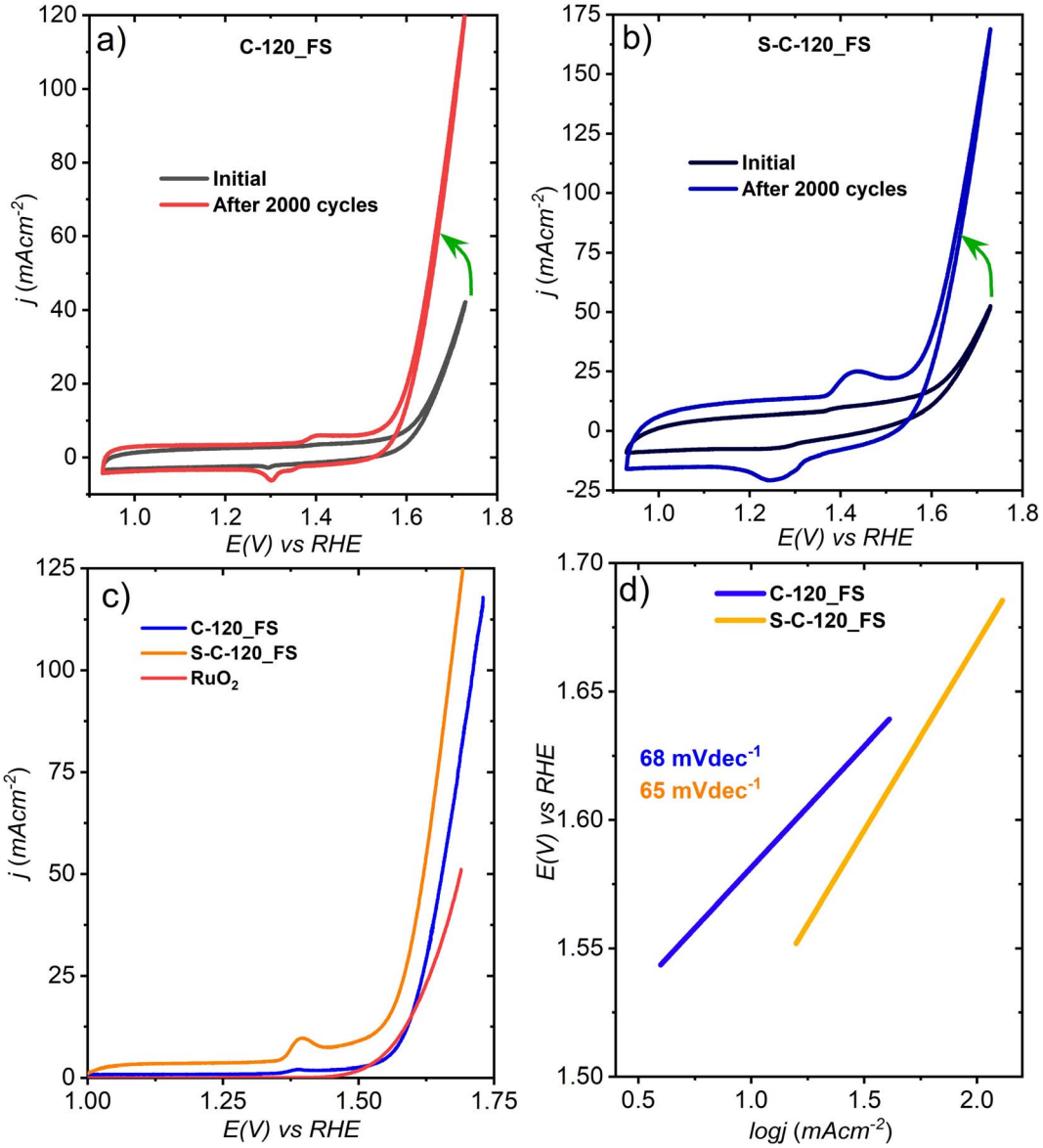

Fig. 3 CVs of (a) C-120_FS and (b) S-C-120_FS and (c) linear sweep voltammetry (LSV) and (d) Tafel plots of the two delaminated FS electrodes.

We then performed LSV of the sulfur-doped ground samples and observed a different trend (Fig. S11b†). The S-C-10, S-C-30, S-C-60 and S-C-120 powders reached the same current density of 10 mA cm^{-2} at a respective overpotential of 420, 470, 480 and 400 mV, clearly indicating a significant effect of sulfur on OER activity. Among these samples, S-C-120 outperformed the other synthesized materials in terms of lower overpotential, with the activity trend being:

$$\text{S-C-120} > \text{S-C-10} > \text{S-C-30} > \text{S-C-60}.$$

For all powder samples, we analyzed the kinetics of the synthesized delaminated electrodes using the Tafel equation [$\eta = a + b \times \log j$] with a = constant, $b = 2.3RT/\alpha F$, and j = current density. We carried out LSV with a rotating disk electrode (RDE) at 1600 rpm at a scan rate of 5 mV s^{-1}. The ohmic drop corrected Tafel slopes were 51, 55, 61 and 58 mV dec^{-1} for the non-doped C-10, C-30, C-60 and C-120, respectively (Fig. S11c†). C-10 showed faster kinetics while oxidizing water. The sulfur-doped S-C-10, S-C-30, S-C-60 and S-C-120 exhibited slopes of 57, 54, 75 and 50 mV dec^{-1} with the smaller Tafel slope of S-C-120 validating its improved OER kinetics (Fig. S11d†).

Experiments with free-standing electrodes show good performance. We also tested the freestanding (FS) electrodes synthesized for 2 hours (C-120_FS and S-C-120_FS), since they showed sufficient mechanical strength to withstand electrocatalysis (the samples processed for less than two hours did not exhibit sufficient mechanical strength for proper contact with the electrode or to endure the electrocatalysis). The activity of the FS electrodes was evaluated in an alkaline electrolyte (1 M KOH). For the comparison, we used RuO_2 loaded on carbon

paper (1 mg cm^{-2}) as a freestanding electrode. We performed cyclic voltammetry to understand the redox nature of the synthesized C-120_FS and S-C-120_FS. Fig. 3a shows the CVs of C-120_FS and S-C-120_FS that were measured after *I–V* polarization (100 CV cycles were carried out in both cases). Initially, C-120_FS exhibited a characteristic oxidation peak at 1.39 V *vs.* RHE and a reduction peak at 1.29 V *vs.* RHE, which could be due to the redox couple of Ni.[47] However, after 2000 CV cycles, it showed an oxidation peak at 1.41 *vs.* RHE and the same value (1.29 V *vs.* RHE) for the reduction peak (Fig. 3a). S-C-120_FS showed a Ni oxidation peak at 1.4 V *vs.* RHE and a reduction peak at 1.25 V *vs.* RHE. After 2000 CV cycles, the reduction peak remained at the same potential as the initial cycle, while the oxidation peak of Ni shifted to 1.42 V (Fig. 3b).

As previously mentioned, the performance of the sulfur-doped FS electrode was much better compared to the pristine electrode, likely due to the improved electronic conductivity due to S-doping (from impedance measurements). Furthermore, we noticed the dissolution of gold into the electrolyte solution (see Fig. S10 and S20†), consistent with the report that Au dissolution starts at 1.2 V *vs.* RHE in an alkaline solution.[48] After 500 cycles, we noticed a gradual color change of the electrolyte from shiny yellow to dark red (optical images are shown in Fig. S10†) as Au atoms or nanoparticles detach from the carbon. We can speculate that this leads to defects on the carbon matrix that further activate the surface to better catalyze the OER.

LSV that was carried out at 5 mV s^{-1} suggests that S-C-120_FS delivered a benchmarking current density of 10 mA cm^{-2} at an overpotential (η) of 300 mV and showed much higher OER activity than C-120_FS, which exhibited η @10 mA cm^{-2} = 350 mV (Fig. 3c). S-C-120_FS and C-120_FS delivered a current density of 50 mA cm^{-2} at the corresponding η of 380 and 420 mV. S-C-120_FS and C-120_FS reached a *j* of 100 mA cm^{-2} at the respective overpotentials of 430 and 470 mV. Further, the OER activity of S-C-120_FS and C-120_FS outperformed the OER activity of state-of-the-art RuO_2. RuO_2 reached a current density of 10 mA cm^{-2} at an overpotential of 340 mV. We studied the reaction kinetics using their corresponding Tafel plots extracted from the LSV curves, as shown in Fig. 3d. S-C-120_FS exhibited a smaller Tafel slope of 65 mV dec^{-1}, while C-120_FS exhibited a slightly higher slope of 68 mV dec^{-1}. We can speculate that the higher slopes of the FS samples compared to the same samples from powders could be due to the formation of large gas bubbles attached to the electrode surface.

The electrochemically active surface area (ECSA) is a useful descriptor for an electrocatalyst. The ECSA can be calculated as ECSA = C_{dl}/C_s, where C_s is the specific capacitance of the electrode (the C_s value can be 0.04 mF cm^{-2} in 1 M KOH as per reports[49]) and C_{dl} denotes the double-layer capacitance, which is assessed from CV measurements at different sweep rates carried out in the non-faradaic regions (no interfacial charge transfer), as depicted in Fig. S12.† C-120_FS exhibited a C_{dl} of 98 mF cm^{-2}, whereas S-C-120_FS exhibits a much higher C_{dl} of 257 mF cm^{-2}, as shown in Fig. 4a and their corresponding ECSAs are 2450 and 6425 cm^2. Thus, S-doping not only lowers the overpotential, but also significantly enhances the ECSA.

We assessed the stability of S-C-120_FS using potentiostatic chronoamperometry. We applied a potential of 1.61 V *vs.* RHE (corresponding j = 50 mA cm^{-2}) to observe the change in current density over time. As we can see in Fig. 4b, the current became steady nearly after 2.5 h to deliver 50 mA cm^{-2}, showing excellent stability up to 24 hours (with a slight degradation). After 50 h of constant electrolysis, the current density retained is 68% of its initial value. The interruption and reduction of *j* occurred after 24 hours and this could be attributed to the accumulation of the formed O_2 gas bubbles at the surface of the electrode or to the constant Au release into the electrolyte, which eventually reduced the conductivity of 1 M KOH. It is reported that the design of superhydrophobic surfaces could assist in bubble detachment, thus making the electrode more robust.[50] Contact angle measurements revealed that S-C-120_FS was almost superhydrophobic (143.2°; Fig. S17†), which could be the reason for its remarkable stability. The OER durability of the electrode is shown by LSV after 5000 CV cycles, which exhibited negligible loss of potential (Fig. S16†). We also tested the OER durability of the electrode for about 20 000 cycles and observed a large change in potential ($\Delta\eta$ at 25 mA cm^{-2} = 80 mV) in the same electrolyte; however, when we switched to a fresh electrolyte, we observed a very pronounced activity with negligible loss in potential ($\Delta\eta$ at 25 mA cm^{-2} = 10 mV), better than what we observed after 5000 cycles.

In the initial cycles, S-C-120_FS exhibited high charge transfer resistances, given that the diameter of the semicircle in the Nyquist plot is quite large, leading to poor conductivity and slower OER kinetics (Fig. 4c). However, after 2000 cycles, S-C-120_FS became significantly active towards faradaic reactions, as shown in the Nyquist plot (Fig. 4d). The distance between the high frequency and low frequency regions is greatly reduced (a smaller arc of semicircles), indicating better charge transfer resistance and improved electronic conductivity. The two types of semicircles observed for S-C-120_FS can be attributed to the presence of two time constants (see the Bode plot in Fig. S17† and the equivalent circuit with fitting parameters in Fig. S18†).

Hydrogen evolution reaction (HER)

We assessed the HER catalytic performance of the FS electrodes in a 1 M KOH electrolyte saturated by purging 99.9% Ar gas for about 30 min. To compare our performance with a known reference, we used 10% Pt/C loaded on carbon paper (1 mg cm^{-2}) a freestanding electrode. Initially, just after *I–V* polarization (after 100 CV cycles at 50 mVs^{-1}), C-120_FS and S-C-120_FS showed large HER onset overpotentials of 400 and 340 mV at the current densities of 11 and 18 mA cm^{-2}, respectively (Fig. 5a). The performance improvement by S-C-120_FS compared to C-120_FS proved its better suitability for the HER. While testing the electrode for 20 000 cycles to check its robustness under alkaline conditions, surprisingly, we observed a dramatic enhancement of the performance, as shown in Fig. 5a. After 20 000 cycles, S-C-120_FS showed a low onset overpotential of 40 mV at 17 mA cm^{-2} and reached a *j* of 50 mA cm^{-2} and 100 mA cm^{-2} at low overpotentials of 123 and 195 mV, respectively. The noble Pt/C (10% Pt) reached a *j* of 10

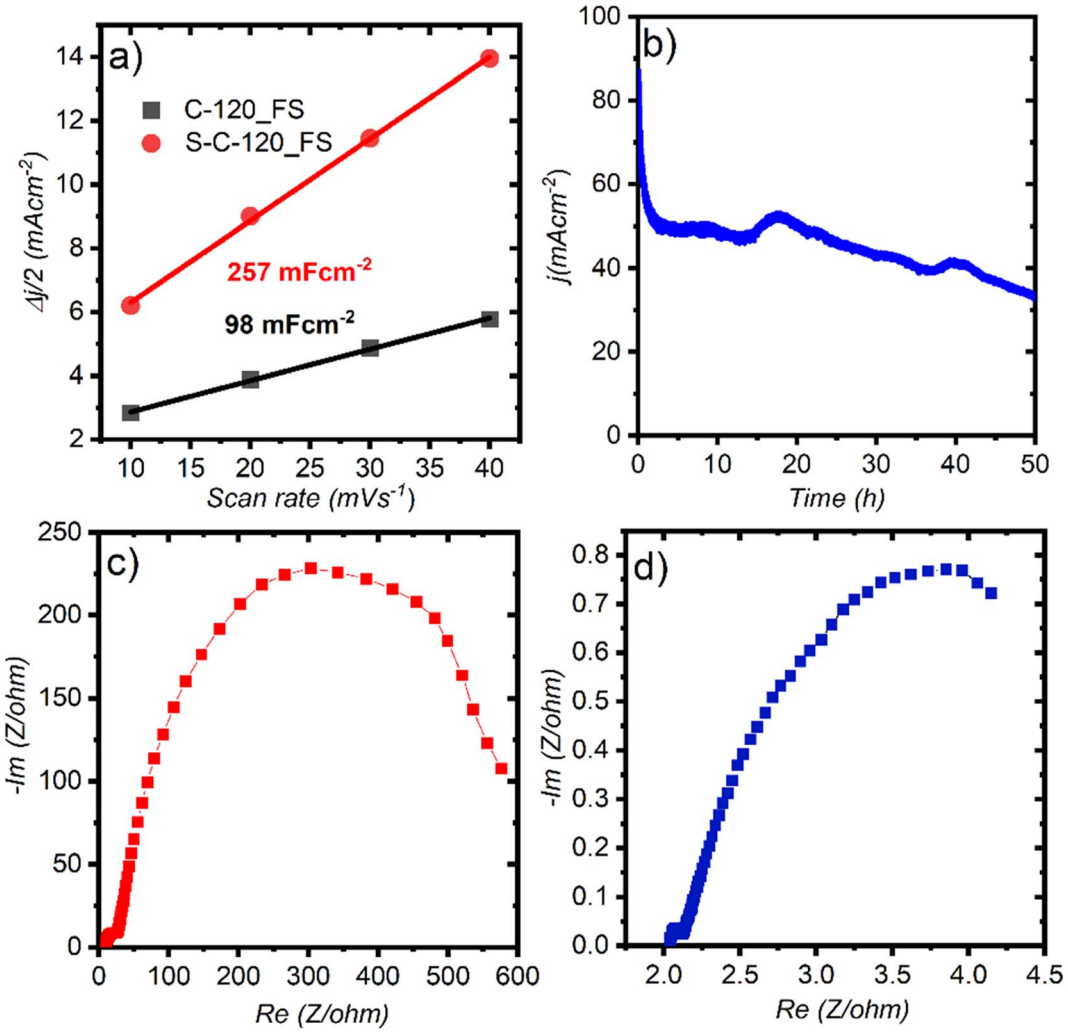

Fig. 4 (a) Double layer capacitance plots of delaminated FS electrodes and (b) long term chronoamperometry of S-C-120_FS. Nyquist plots of S-C-120_FS from EIS (c) in the initial cycles and (d) after 2000 cycles.

mA cm^{-2} at an overpotential of 65 mV. 10% Pt/C further achieved a j of 50 mA cm^{-2} and 100 mA cm^{-2} at overpotentials of 205 mV and 300 mV, respectively. These results indicate that after 20 k cycles, S-C-120_FS showed outstanding HER activity, which outperformed precious Pt. The Tafel slopes of 305, 283 and 285 mV dec^{-1} were observed for C-120_FS, S-C-120_FS and S-C-120_FS after 20 000 cycles (Fig. 5b). We carried out electrolysis under static conditions and observed large and non-linear Tafel slopes due to the accumulation of gas bubbles and the existence of mass transfer effects, thus failing to display the actual kinetics of the catalysts.

EIS spectra after 20 k cycles revealed that S-C-120_FS showed a much smaller semicircle than the initial cycles of S-C-120_FS and C-120_FS, thus indicating better conductivity after 20 k cycles (Fig. 5c). We observed two atypical incomplete semicircles in these three cases: one small semicircle at higher frequency representing bulk electrolyte resistance and a large semicircle formed at lower frequency representing the charge transfer resistance owing to H_2 evolution. We performed chronoamperometry to study the stability of the electrode after 20 k cycles (Fig. 5d). The electrode showed good HER stability over 100 h of electrolysis at a high current density of 100 mA cm^{-2} (η of 195 mV), with the j retained at 80%, with the current drop possibly caused by the accumulation of gaseous bubbles. Overall, the results imply that the diffusion of the electrolyte into the electrodes (for wetting) took a longer time to activate the electrodes (~2500 CV cycles at 20 mVs^{-1}) and to allow the reactant species (H_2O) to reach the catalytically active sites.

Discussion on electrocatalytic activity enhancement

Contact angle measurements before electrocatalysis showed an average angle of 128.76° for C-120 and of 143.23° for S-C-120, a value close to super-hydrophobicity (Fig. S16†). However, post-electrocatalysis contact angle measurements showed a dramatic change in wettability, with the electrodes becoming very hydrophilic (Fig. S16c and d†). We can correlate this change in hydrophobicity to the increased electrocatalytic activity of S-C-120 during cycling. As the formed delaminated electrodes are

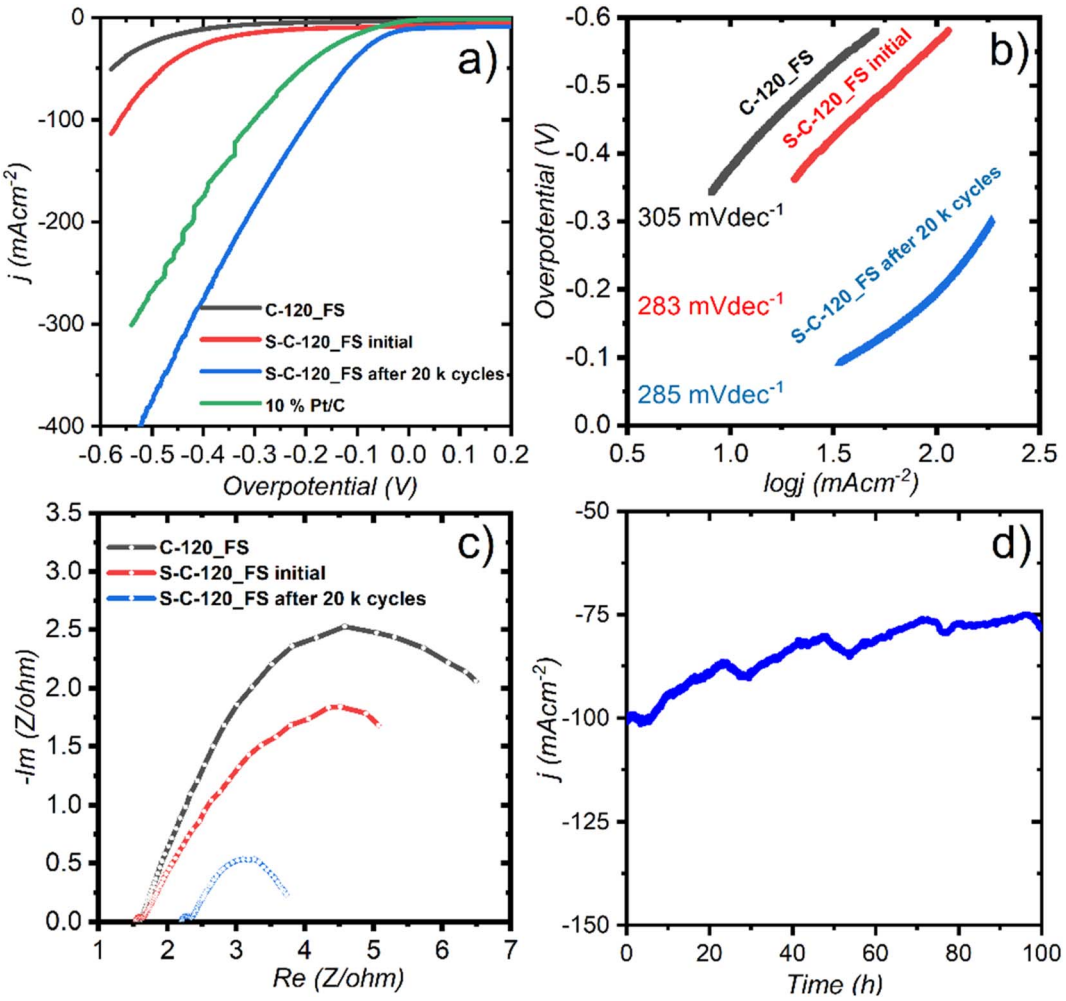

Fig. 5 (a) Results of *iR*-corrected linear sweep voltammetry carried out at 5 mV s^{-1}. (b) Tafel slopes calculated from LSV using the Tafel equation, (c) Nyquist plot obtained from EIS measurement and (d) CA test results of the activated S-C-120_FS.

very hydrophobic in nature, the diffusivity of water molecules (particularly reactants; OH^-) is slower in the initial cycles and only the top layers of the electrode (catalysts) get access to the reactant species. As time progresses, the reactant species can reach more active sites inside the carbon matrix, thus delivering high current densities with lower overpotentials in both the OER and the HER. As can be inferred from CV results (Fig. 3b), the Ni oxidation/reduction peak is not noticeable in the initial cycles (after 100 cycles of *I*–*V* polarization), but is well noticed after only 2000 CV cycles. Additionally, Au dissolution was undetectable in the initial cycles as OH^- species could only reach Au sites on the surface of the carbon matrix (and not the Au sites inside). As diffusion is a time dependent phenomenon, after 500 CV cycles (anodic reaction), Au atoms begin to dissolve into the electrolytic solution and progressively continue to be released over cycling. The recorded OER results after 20 000 cycles reveal pronounced catalytic activity after replacing the electrolyte (1 M KOH solution). After 2000 CV cycles of the OER, we carried out HR-SEM, contact angle, and XRD measurements. HR-SEM images clearly revealed that pores and cavities were formed as a result of partial Au removal, which created pathways for the movement of electroactive species (Fig. S21†). More importantly, post-XRD proves that the crystallinity of the carbon matrix remained unaffected, which is evidence of the corrosion-resistant ability of the S-C-120 electrodes (Fig. 2c). Reports suggest that improving crystallinity helps the corrosion resistance of carbon.[51] We could possibly relate the enhanced OER activity shown by S-C-120 to the improvement of wettability upon time and the formation of holes and large cavities or defects in the carbon matrix, thus providing more open access of the OH^- species to the catalytically active Ni sites inside the carbon matrix. Based on the observed phenomena, we have postulated a scheme that demonstrates the possible mechanism of electrode activation, which could be a factor for high OER activity, as depicted in Fig. 6. On the cathodic side (HER), we did not observe the dissolution of Au since Au is stable at negative potentials. In this case, we could relate the improved performance to the diffusivity of water molecules to active sites after prolonged cycling. We speculate that both Ni and Au act as prime catalytic sites for the HER supported by S-doped carbon. We examined the Brunauer–Emmett–Teller (BET) surface area of pristine, post-OER and post-HER samples (Fig. S22†). Pristine

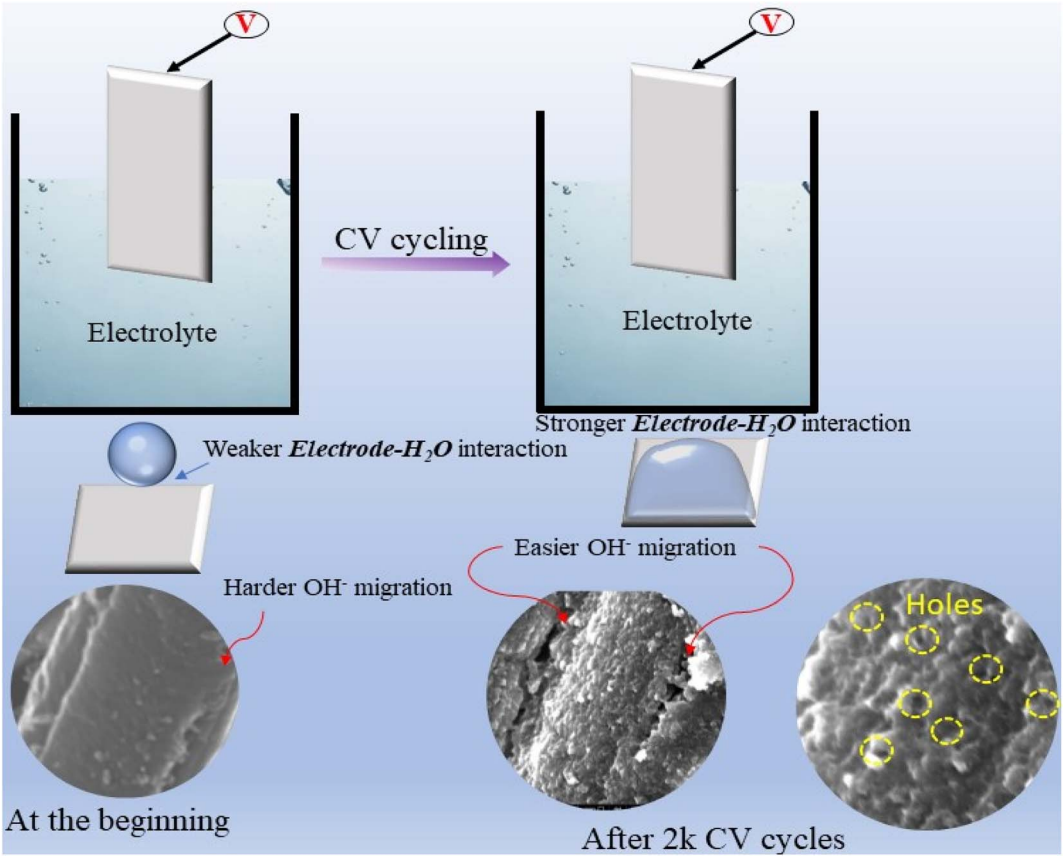

Fig. 6 Schematic demonstrating the plausible mechanism of electrode activation during OER cycling.

S-C-120 exhibited a BET surface area and an average pore diameter of 26.712 $m^2\ g^{-1}$ and 36.4 Å, respectively. Post-OER BET showed a noticeable increase in the surface area (31.5 $m^2\ g^{-1}$) and an average pore diameter (43 Å), thus indicating the enlargement of pores due to Au removal. Post-HER BET showed smaller deviations in the surface area (24.04 $m^2\ g^{-1}$) and an average pore diameter (39.47 Å) (detailed parameters are given in Table S1†).

Post-characterization

We performed aberration-corrected HRTEM of the electrodes after 2000 OER CV cycles and observed noticeable defects and pores, as some of the Au was removed from the electrode (Fig. S17 and S18†). The HAADF-STEM images demonstrated a uniform presence of carbon and a much higher presence of Ni than Au. XPS was carried out for both post-OER and HER samples.

The survey spectrum after the OER showed the presence of O, C, S and Ni (see the zoomed-in spectra of Fig. S19†) and additionally K (K 2s at 378.2 eV, K 2p at 293.4 and 296.2 eV, K 3 s at 33.8 eV and K 3p at 17.6 eV) was also present (Fig. S19†). The C 1s spectrum can be fitted with four peaks at 284.5 eV (adventitious carbon), 284.7 eV (carbon in the matrix of the material), 285.6 eV (carbon bound to S) and 288.15 eV (C═O). The S 2p doublet at 164 eV is compatible with S bound to C (thiophene type), while the S 2p doublet at 168.3 eV can be attributed to SO_x species. Ni likely exists in an +3 state, as evidenced by the presence of a $3p_{3/2}$ characteristic peak at 69.05 eV.[52,53] The O 1s spectrum can be fitted to three peaks at 531.4, 533.15 and 535.15 eV due to M–O, M–OH and M–H_2O bonding, respectively.

In the survey spectrum, after the HER we detected O, C, S and Ni (see zoomed-in spectra, Fig. S20†). The C 1s spectrum can be fitted with three peaks at 284.45 eV (adventitious carbon), 284.7 eV (carbon in the matrix of the material) and 285.5 eV (carbon bound to S). The S 2p doublet at 163.75 eV is compatible with S bound to C, while the S 2p doublet at 168 eV can be attributed to SO_x species. Ni in this case exists in a +2 oxidation state where the observed peak is positioned at 68.25 eV.[53] The O 1s spectrum can be fitted with two peaks at 531.7 and 532.2 eV, which can be attributed to metal–oxygen or carbon–oxygen bonding.

Water splitting performance comparison

To replace PGM-based electrocatalysts, numerous self-supported electrodes have been developed based on earth-abundant metals. In this regard, binder-free electrodes not only provide higher electrocatalytic activity, but also show improved stability due to the high surface area and departure of gas bubbles from the electrode surface. The bi-functional (HER and OER) electrocatalytic activity of S-C-120_FS compared to other previously studied self-supported electrodes is given in

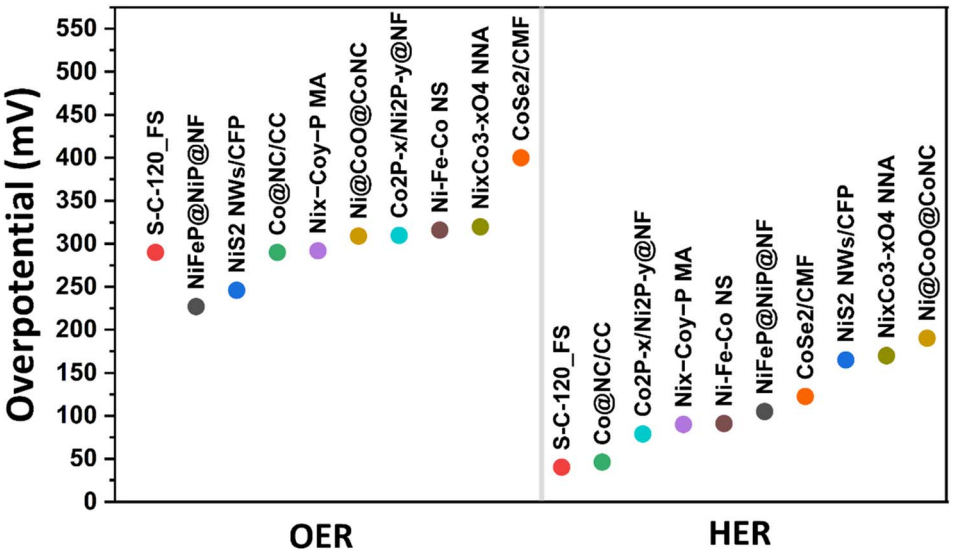

Fig. 7 The HER and OER electrocatalytic performance comparisons between our electrode with other reported freestanding electrodes that are examined in 1 M KOH electrolyte (overpotential *vs.* current density @10 mA cm^{-2}).

Fig. 7. In most cases, the HER activity of S-C-120_FS outperforms the HER activity in earlier reports, which shows the superiority of S-C-120_FS as a HER catalyst, while exhibiting OER performance comparable with those of other catalysts. The compared bi-function catalysts for the OER and HER are termed NiS_2 NWs/CFP,[54] Co_2P-*x*/Ni_2P-*y*@NF,[55] NiFeP@NiP@NF,[56] Ni_x–Co_y–P microarrays,[57] $CoSe_2$/CMF,[58] Ni–Fe–Co nanostructure, $Ni_xCo_{3-x}O_4$ nanoneedle arrays,[59] Co@NC/CC,[60] and Ni@CoO@CoNC.[61]

Conclusion

We designed a simple, one step CVD synthesis based on a new paradigm of thermal delamination of a thin film stack to synthesize Ni SACs anchored on a CNF mat as free-standing electrodes. The sulfur-doped, 2 h grown electrode outperformed the overall water splitting performance of the same non-doped material. It exhibited low onset overpotential, high current density, outstanding durability, and a remarkable ECSA for both the OER and the HER with cycling performance for 20 000 cycles.

Many physicochemical effects are at are involved in delivering this material, including thermal delamination of thin metal films *via* a weak adhesion layer, the nucleation and growth of carbon nanofibers, subsequent sulfur doping, the formation of Ni and Au SACs, and changes in hydrophobicity during cycling. We believe that this new paradigm of thermal delamination of thin films to grow catalyst atoms on a doped nanocarbon matrix could open new research avenues to produce high-performance, low-cost electrodes for various electrochemical applications.

Data availability

The data supporting this article have been included as part of the ESI.†

Conflicts of interest

There are no conflicts of interest.

Acknowledgements

The authors thank Dr Olga Girshevitz for helping with RBS measurements and Dr Yuval Elias for editing. The authors thankfully acknowledge a Kamin Grant from the Israel Innovation Authority #77822 for partial funding. We acknowledge Dr Paolo Moras for assistance in the experiments at the VUV-photoemission beamline (Elettra, Trieste).

References

1 B. Zhao, J. Liu, X. Wang, C. Xu, P. Sui, R. Feng, L. Wang, J. Zhang, J. L. Luo and X. Z. Fu, *Nano Energy*, 2021, **80**, 105530.
2 B. Malik, K. Vijaya Sankar, S. K. T. Aziz, S. Majumder, Y. Tsur and G. D. Nessim, *J. Phys. Chem. C*, 2021, **125**, 23126–23132.
3 B. Malik, S. Majumder, R. Lorenzi, I. Perelshtein, M. Ejgenberg, A. Paleari and G. D. Nessim, *ChemPlusChem*, 2022, **87**, e202200036.
4 S. Kundu, B. Malik, D. K. Pattanayak, P. Ragupathy and V. K. Pillai, *ChemistrySelect*, 2017, **2**, 9943–9946.
5 S. Kundu, B. Malik, A. Prabhakaran, D. K. Pattanayak and V. K. Pillai, *Chem. Commun.*, 2017, **53**, 9809–9812.
6 B. Malik, K. Vijaya Sankar, R. Konar, Y. Tsur and G. D. Nessim, *ChemElectroChem*, 2021, **8**, 517.
7 K. S. Exner and H. Over, *ACS Catal.*, 2019, **9**, 6755–6765.
8 C. Roy, R. R. Rao, K. A. Stoerzinger, J. Hwang, J. Rossmeisl, I. Chorkendorff, Y. Shao-Horn and I. E. L. Stephens, *ACS Energy Lett.*, 2018, **3**, 2045–2051.
9 S. Kundu, B. Malik, D. K. Pattanayak and V. K. Pillai, *ChemElectroChem*, 2018, **5**, 1670–1676.
10 A. Wang, J. Li and T. Zhang, *Nat. Rev. Chem*, 2018, **2**, 65–81.

11 M. Luo, W. Sun, B. Bin Xu, H. Pan and Y. Jiang, *Adv. Energy Mater.*, 2021, **11**, 1–14.
12 M. B. Gawande, P. Fornasiero and R. Zbořil, *ACS Catal.*, 2020, **10**, 2231–2259.
13 Y. Zhou, G. Gao, Y. Li, W. Chu and L. W. Wang, *Phys. Chem. Chem. Phys.*, 2019, **21**, 3024–3032.
14 Z. Zhang, C. Feng, C. Liu, M. Zuo, L. Qin, X. Yan, Y. Xing, H. Li, R. Si and S. Zhou, *Nat. Commun.*, 2020, **11**, 1–8.
15 X. Lv, W. Wei, H. Wang, B. Huang and Y. Dai, *Appl. Catal., B*, 2020, **264**, 118521.
16 Y. Qu, L. Wang, Z. Li, P. Li, Q. Zhang, Y. Lin, F. Zhou, H. Wang, Z. Yang, Y. Hu, M. Zhu, X. Zhao, X. Han, C. Wang, Q. Xu, L. Gu, J. Luo, L. Zheng and Y. Wu, *Adv. Mater.*, 2019, **31**, 1–7.
17 H. Fei, J. Dong, Y. Feng, C. S. Allen, C. Wan, B. Volosskiy, M. Li, Z. Zhao, Y. Wang, H. Sun, P. An, W. Chen, Z. Guo, C. Lee, D. Chen, I. Shakir, M. Liu, T. Hu, Y. Li, A. I. Kirkland, X. Duan and Y. Huang, *Nat. Catal.*, 2018, **1**, 63–72.
18 H. Xu, T. Liu, S. Bai, L. Li, Y. Zhu, J. Wang, S. Yang, Y. Li, Q. Shao and X. Huang, *Nano Lett.*, 2020, **20**, 5482–5489.
19 J. Zhang, C. Liu and B. Zhang, *Small Methods*, 2019, **3**, 1–15.
20 S. S. A. Shah, T. Najam, M. S. Javed, M. S. Bashir, M. A. Nazir, N. A. Khan, A. ur Rehman, M. A. Subhan and M. M. Rahman, *Chem. Rec.*, 2022, **22**, e202100280.
21 J. Guo, H. Liu, D. Li, J. Wang, X. Djitcheu, D. He and Q. Zhang, *RSC Adv.*, 2022, **12**, 9373–9394.
22 H. Xu, Y. Zhao, Q. Wang, G. He and H. Chen, *Coord. Chem. Rev.*, 2022, **451**, 214261.
23 J. Kwon, H. Han, S. Choi, K. Park, S. Jo, U. Paik and T. Song, *ChemCatChem*, 2019, **11**, 5898–5912.
24 T. Y. Ma, S. Dai and S. Z. Qiao, *Mater. Today*, 2016, **19**, 265–273.
25 X. Lv, W. Wei, H. Wang, B. Huang and Y. Dai, *Appl. Catal., B*, 2020, **264**, 118521.
26 G. D. Nessim, M. Seita, K. P. O'Brien, A. J. Hart, R. K. Bonaparte, R. R. Mitchell and C. V Thompson, *Nano Lett.*, 2009, **9**, 3398–3405.
27 A. Itzhak, E. Teblum, O. Girshevitz, S. Okashy, Y. Turkulets, L. Burlaka, G. Cohen-Taguri, E. Shawat Avraham, M. Noked and I. Shalish, *Chem. Mater.*, 2018, **30**, 2379–2388.
28 G. F. Li, D. Yang and P. Y. Abel Chuang, *ACS Catal.*, 2018, **8**, 11688–11698.
29 H. A. Miller, K. Bouzek, J. Hnat, S. Loos, C. I. Bernäcker, T. Weißgärber, L. Röntzsch and J. Meier-Haack, *Sustainable Energy Fuels*, 2020, **4**, 2114–2133.
30 P. Wang and B. Wang, *ChemSusChem*, 2020, **13**, 4795–4811.
31 E. Shawat, I. Perelshtein, A. Westover, C. L. Pint and G. D. Nessim, *J. Mater. Chem. A*, 2014, **2**, 15118–15123.
32 R. F. Wolffenbuttel and K. D. Wise, *Sens. Actuators, A*, 1994, **43**, 223–229.
33 W. Wan, Y. Zhao, S. Wei, C. A. Triana, J. Li, A. Arcifa, C. S. Allen, R. Cao and G. R. Patzke, *Nat. Commun.*, 2021, **12**, 1–13.
34 D. A. L. Almeida, A. B. Couto, S. S. Oishi and N. G. Ferreira, *J. Solid State Electrochem.*, 2018, **22**, 3493–3505.
35 P. Ghosh, T. Soga, K. Ghosh, T. Jimbo, R. Katoh, K. Sumiyama and Y. Ando, *Nanoscale Res. Lett.*, 2008, **3**, 242.
36 M. C. Biesinger, *Appl. Surf. Sci.*, 2022, **597**, 153681.
37 X. Xing, R. Liu, M. Anjass, K. Cao, U. Kaiser, G. Zhang and C. Streb, *Appl. Catal., B*, 2020, **277**, 119195.
38 C. Qi, X. Ma, G. Ning, X. Song, B. Chen, X. Lan, Y. Li, X. Zhang and J. Gao, *Carbon*, 2015, **92**, 245–253.
39 B. P. Payne, M. C. Biesinger and N. S. McIntyre, *J. Electron Spectrosc. Relat. Phenom.*, 2009, **175**, 55–65.
40 H. Liu, M. X. Wu and S. N. Ding, *Biosensors*, 2022, **12**, 797.
41 G. W. Ho, A. T. S. Wee, J. Lin and W. C. Tjiu, *Thin Solid Films*, 2001, **388**, 73–77.
42 M. Chhowalla, K. B. K. Teo, C. Ducati, N. L. Rupesinghe, G. A. J. Amaratunga, A. C. Ferrari, D. Roy, J. Robertson and W. I. Milne, *J. Appl. Phys.*, 2001, **90**, 5308–5317.
43 F. Hassani and H. Tavakol, *Fullerenes, Nanotubes Carbon Nanostruct.*, 2018, **26**, 479–486.
44 W. Li, D. Yang, H. Chen, Y. Gao and H. Li, *Electrochim. Acta*, 2015, **165**, 191–197.
45 A. M. El-Sawy, I. M. Mosa, D. Su, C. J. Guild, S. Khalid, R. Joesten, J. F. Rusling and S. L. Suib, *Adv. Energy Mater.*, 2016, **6**, 1501966.
46 L. Zhang, Y. Hu, K. Jiang, K. Li, Y.-Q. Liu, D. Wang and Y. Ye, *J. Electrochem. Soc.*, 2021, **168**, 054523.
47 J. Li, Z. Luo, F. He, Y. Zuo, C. Zhang, J. Liu, X. Yu, R. Du, T. Zhang, M. F. Infante-Carrió, P. Tang, J. Arbiol, J. Llorca and A. Cabot, *J. Mater. Chem. A*, 2018, **6**, 22915–22924.
48 S. Cherevko, A. R. Zeradjanin, G. P. Keeley and K. J. J. Mayrhofer, *J. Electrochem. Soc.*, 2014, **161**, H822–H830.
49 C. C. L. McCrory, S. Jung, J. C. Peters and T. F. Jaramillo, *J. Am. Chem. Soc.*, 2013, **135**, 16977–16987.
50 A. Angulo, P. van der Linde, H. Gardeniers, M. Modestino and D. Fernández Rivas, *Joule*, 2020, **4**, 555–579.
51 M.-G. Kim, T. K. Lee, E. Lee, S. Park, H. J. Lee, H. Jin, D. W. Lee, M.-G. Jeong, H.-G. Jung, K. Im, C. Hu, H. C. Ham, K. H. Song, Y.-E. Sung, Y. M. Lee and S. J. Yoo, *Energy Environ. Sci.*, 2023, **16**, 5019–5028.
52 C. L. McBean, H. Liu, M. E. Scofield, L. Li, L. Wang, A. Bernstein and S. S. Wong, *ACS Appl. Mater. Interfaces*, 2017, **9**, 24634–24648.
53 M. Burriel, S. Wilkins, J. P. Hill, M. A. Muñoz-Márquez, H. H. Brongersma, J. A. Kilner, M. P. Ryan and S. J. Skinner, *Energy Environ. Sci.*, 2014, **7**, 311–316.
54 Y. Guo, D. Guo, F. Ye, K. Wang and Z. Shi, *Int. J. Hydrogen Energy*, 2017, **42**, 17038–17048.
55 H. Zhao, J. Liang and Y. Zhao, *J. Alloys Compd.*, 2022, **907**, 164479.
56 F. Diao, W. Huang, G. Ctistis, H. Wackerbarth, Y. Yang, P. Si, J. Zhang, X. Xiao and C. Engelbrekt, *ACS Appl. Mater. Interfaces*, 2021, **13**, 23702–23713.
57 X. X. Liu, Q. He, S. Xiao, X. Li, L. Chang, Y. Xiang, K. Hu, X. Niu, R. Wu and J. S. Chen, *ChemElectroChem*, 2021, **8**, 1307–1315.
58 Y. Wang, J. Yu, Q. Liu, J. Liu, R. Chen, J. Zhu, R. Li and J. Wang, *Electrochim. Acta*, 2023, **438**, 141594.
59 Gh. Barati Darband, M. Aliofkhazraei and A. S. Rouhaghdam, *J. Colloid Interface Sci.*, 2019, **547**, 407–420.
60 J. Bao, W. Liu, J. Xie, L. Xu, M. Guan, F. Lei, Y. Zhao, Y. Huang, J. Xia and H. Li, *Chem.–Asian J.*, 2019, **14**, 480–485.
61 Q. Jia, Y. Gao, Y. Li, X. Fan, F. Zhang, G. Zhang, W. Peng and S. Wang, *Carbon*, 2019, **155**, 287–297.